JACS
JOURNAL OF THE AMERICAN CHEMICAL SOCIETY

Article

pubs.acs.org/JACS

Mn(II) Oxidation by the Multicopper Oxidase Complex Mnx: A Binuclear Activation Mechanism

Alexandra V. Soldatova,[†] Lizhi Tao,[#,‡] Christine A. Romano,[§,‡] Troy A. Stich,[#] William H. Casey,[#,⊥] R. David Britt,[#] Bradley M. Tebo,[§] and Thomas G. Spiro*[,†]

[†]Department of Chemistry, University of Washington, Box 351700, Seattle, Washington 98195, United States

[§]Division of Environmental and Biomolecular Systems, Institute of Environmental Health, Oregon Health & Science University, Portland, Oregon 97239, United States

[#]Department of Chemistry and [⊥]Earth and Planetary Sciences Department, University of California, Davis, One Shields Avenue, Davis, California 95616, United States

Supporting Information

ABSTRACT: The bacterial protein complex Mnx contains a multicopper oxidase (MCO) MnxG that, unusually, catalyzes the two-electron oxidation of Mn(II) to MnO_2 biomineral, via a Mn(III) intermediate. Although Mn(III)/Mn(II) and Mn(IV)/Mn(III) reduction potentials are expected to be high, we find a low reduction potential, 0.38 V (vs Normal Hydrogen Electrode, pH 7.8), for the MnxG type 1 Cu^{2+}, the electron acceptor. Indeed the type 1 Cu^{2+} is not reduced by Mn(II) in the absence of molecular oxygen, indicating that substrate oxidation requires an activation step. We have investigated the enzyme mechanism via electronic absorption spectroscopy, using chemometric analysis to separate enzyme-catalyzed MnO_2 formation from MnO_2 nanoparticle aging. The nanoparticle aging time course is characteristic of nucleation and particle growth; rates for these processes followed expected dependencies on Mn(II) concentration and temperature, but exhibited different pH optima. The enzymatic time course is sigmoidal, signaling an activation step, prior to turnover. The Mn(II) concentration and pH dependence of a preceding lag phase indicates weak Mn(II) binding. The activation step is enabled by a pK_a > 8.6 deprotonation, which is assigned to Mn(II)-bound H_2O; it induces a conformation change (consistent with a high activation energy, 106 kJ/mol) that increases Mn(II) affinity. Mnx activation is proposed to decrease the Mn(III/II) reduction potential below that of type 1 Cu(II/I) by formation of a hydroxide-bridged binuclear complex, Mn(II)(μ-OH)Mn(II), at the substrate site. Turnover is found to depend cooperatively on two Mn(II) and is enabled by a pK_a 7.6 double deprotonation. It is proposed that turnover produces a Mn(III)(μ-$OH)_2$Mn(III) intermediate that proceeds to the enzyme product, likely Mn(IV)(μ-$O)_2$Mn(IV) or an oligomer, which subsequently nucleates MnO_2 nanoparticles. We conclude that Mnx exploits manganese polynuclear chemistry in order to facilitate an otherwise difficult oxidation reaction, as well as biomineralization. The mechanism of the Mn(III/IV) conversion step is elucidated in an accompanying paper.

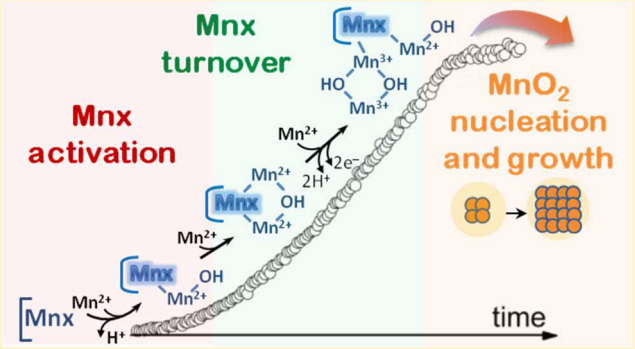

INTRODUCTION

The environmental chemistry of manganese is dominated by microbially mediated redox cycling.[1−5] MnO_2 mineral provides an electron sink for many bacteria, which reduce it to Mn(II).[6−8] MnO_2 is a strong oxidant, but not as strong as O_2, and is therefore the stable form of manganese in an aerobic environment. However, the uncatalyzed oxidation of Mn(II) is very slow at pH conditions of most natural waters, including seawater.[9] Thus, in most geochemical environments, the manganese cycle is closed by the microbial mediation. Many bacteria and fungi are capable of catalyzing this oxidation, and most of the MnO_2 found in soils and sediment are believed to result from biological processing.[1,3−5,10−12]

The physiological function of Mn(II) oxidation and biomineralization—*why* microbes perform these reactions—is unknown. The process may protect cells from reactive oxygen species.[3,13,14] Alternatively, the MnO_2 mineral could be used to degrade complex organic molecules for nutrient production.[15] Or, it could provide protection from environmental stressors such as UV radiation, predation, or phage infection.[1,16] None of these functions, however, have been established for any of the phylogenetically diverse Mn-oxidizing organisms.[17]

In this study, we address the question of *how* the conversion of Mn(II) to MnO_2 is accomplished biochemically. The reason

Received: March 22, 2017
Published: July 17, 2017

DOI: 10.1021/jacs.7b02771
J. Am. Chem. Soc. 2017, 139, 11369−11380

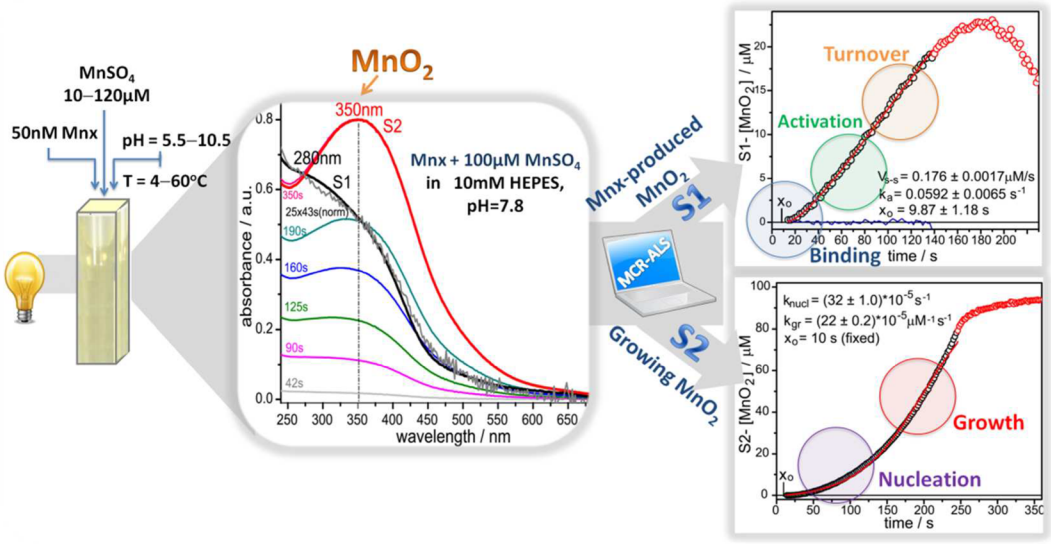

Figure 1. Schematic illustrating experimental approach employed in the current study. UV−vis absorption spectrophotometry was used to monitor Mnx-catalyzed Mn(II) oxidation. The reaction product, colloidal MnO_2 (yellow solution in the cuvette), is tracked by its broad absorption band (250−450 nm). The band grows and shifts to longer wavelengths, indicating maturation of the initially formed enzyme product. To separate enzyme catalysis from MnO_2 nanoparticle growth, the MCR-ALS (Multivariate Curve Resolution−Alternating Least-Squares) chemometric technique was employed (see Methods for details), resulting in two components, S1 (enzymatic) and S2 (MnO_2 growth), both having sigmoidal time courses. These were fit with the appropriate equations (see Results and Discussion for details), to obtain kinetic parameters.

for the slow uncatalyzed oxidation is the difficulty of extracting an electron from aquo-Mn(II), owing to stabilization of its half-filled d electronic subshell (d^5). Aquo-Mn(III) has a very high reduction potential, E^0 = 1.5 V,[18,19] and disproportionates to Mn(II) and MnO_2. Mn(III) can, however, be stabilized by strong chelating agents.[19−21] Significant levels of soluble Mn(III) have recently been detected in oxic and suboxic marine waters[22−24] and sediments,[25] presumably reflecting the availability of naturally occurring chelators. The Mn(III)/Mn(II) potential can also be substantially modified by ligation (usually to imidazole and carboxylates) at protein binding sites.[26−29] Nevertheless, lowering it sufficiently to permit electron transfer from Mn(II) is a challenge for oxidative enzymes. In addition, the enzymes must coordinate the transfer of a second electron and generate a lattice of MnO_2 biomineral. Enzymatic oxidation is also involved in the production of iron biominerals: the ferrihydrite-like Fe_2O_3 produced in the internal cavity of the storage protein ferritin,[30−33] and Fe_3O_4 or Fe_3S_4, formed into nanocrystals of magnetosomes, by an orchestrated assembly of proteins in magnetotactic bacteria.[34−36] But in these cases, mineralization involves only one-electron redox chemistry of the lower potential Fe(III)/Fe(II) couple.

Intriguingly, the enzyme responsible for Mn(II) oxidation in a number of bacteria is a multicopper oxidase (MCO).[37−45] MCOs are well-studied enzymes that transfer electrons one at a time from substrates to a unique Cu^{2+} center, the type 1 Cu, which relays the electrons to a trinuclear Cu cluster, composed of one type 2 and two type 3 Cu atoms, where O_2 is reduced to water.[46,47] Substrates of MCOs include a variety of organic molecules, and also Fe^{2+} and Cu^{+}, which undergo single-electron oxidations. But a 2-electron metal-oxidizing MCO is unprecedented. Also unprecedented is a biomineralizing MCO. These manganese oxidases represent a new subclass of MCOs.

The MCO manganese oxidases have been difficult to isolate, but Tebo and co-workers have recently succeeded in obtaining one from marine *Bacillus sp*. Strain PL-12, by expressing four contiguous genes contained as part of an operon conserved in three different Mn(II)-oxidizing *Bacillus* species.[48] The MCO protein, MnxG, was isolated in association with accessory proteins, MnxE and MnxF, of currently unknown function. The protein multimer (called the Mnx complex or Mnx), consists of one subunit of MnxG (138 kDa) and six subunits of the smaller (12 kDa) MnxE and MnxF; it is functional in oxidizing Mn(II).[48−50] MnxG is unique among the known MCOs in having accessory proteins.[51−53]

In this study, we investigate how Mn(II) oxidation by Mnx is managed. We find the reduction potential of the type 1 Cu to be surprisingly low, 380 mV (vs Normal Hydrogen Electrode, NHE, pH 7.8), near the low end of the scale of MCOs. Indeed, it is not reduced by Mn(II) in the absence of O_2, but is reduced in its presence, during turnover. How then does Mn(II) become oxidized during turnover?

To answer this question, we employed UV−vis absorption spectroscopy to perform kinetic measurements of Mnx-catalyzed Mn(II) oxidation, and analyzed the time course, as diagrammed in Figure 1.

The enzyme product undergoes condensation to MnO_2 nuclei, which grow to colloidal nanoparticles. We employed chemometric analysis to separate enzyme catalysis from nanoparticle growth. Both processes have sigmoidal time courses—after a lag phase, a slow initial phase is followed by a fast linear growth. These behaviors indicate that (1) Mnx requires activation to catalyze Mn(II) oxidation, and (2) the growth of MnO_2 particles is preceded by a nucleation step. Both processes were evaluated as functions of starting Mn(II) concentration, pH, and temperature. The possibility that the sigmoidal time courses instead result from abiotic autocatalysis of Mn(II) on the surface of MnO_2 is excluded by showing that successive additions of Mn(II) do not increase the turnover rate, despite the growing concentration of MnO_2.

Among the mechanistic conclusions emerging from these data, the most striking is that the Mnx activation step enables electron transfer by lowering the Mn(III)/Mn(II) reduction

DOI: 10.1021/jacs.7b02771
J. Am. Chem. Soc. 2017, 139, 11369−11380

potential via formation of a binuclear hydroxide-bridged Mn(II) complex, Mn(II)(μ-OH)Mn(II), at the substrate site. A further increase in the driving force occurs during turnover, when a second electron transfer leads to formation of Mn(III)(μ-OH)$_2$Mn(III). In the accompanying paper,[54] we show that this complex is a key intermediate on the path to MnO_2 production, likely through formation of Mn(IV)(μ-O)$_2$Mn(IV). We conclude that Mnx elegantly exploits manganese polynuclear chemistry both to overcome an apparently inadequate driving force and to produce the oxide lattice of biomineralized MnO_2.

METHODS

Spectroscopic Measurements. Manganese-oxidation assays were monitored via absorption spectra obtained with an Agilent (Santa Clara, CA, USA) 8453 UV−vis spectrophotometer, using a thermostatable multicell configuration with automated kinetic scan capability and 10 mm path length cuvettes. The samples were stirred continuously with a Spinette magnetic stirrer (Starna Cells, Atascadero, CA, USA). The temperature was controlled with a Neslab RTE-100 constant temperature water bath. For reactions taking longer than an hour, several assays were monitored in a parallel configuration. For faster reactions, one assay was monitored at a time.

Reaction assays. The Mnx protein complex was purified as previously described.[48,55] Typically, oxidation assays (1 mL volume total) contained 50 nM Mnx in 10 mM HEPES buffer, pH 7.8. For the pH-dependence study, the pH range was 5.55−10.4, and the buffers used were 10 mM MES (pK_a = 6.15), 10 mM HEPES (pK_a = 7.55), and 10 mM CHES (pK_a = 9.36) (see Figure S9 for details). For the temperature-dependence study, HEPES buffer was adjusted to the appropriate pH value for the assay temperature (estimated from the HEPES temperature coefficient of pK_a = −0.014/°C[56]). Mnx stock in the appropriate buffer was equilibrated for 5−10 min in the spectrophotometer cuvette. Then, Mn-oxidation was initiated by adding an aliquot of 0.01 M $MnSO_4$ stock to the cuvette. The cuvette was capped, inverted several times to ensure complete mixing, and returned to the spectrophotometer for measurements. The time for substrate addition and mixing, ∼12−15 s, set time zero for the time course. To process the reaction spectra, the enzyme spectrum was subtracted from the evolving spectra (only a small UV contribution at ∼280 nm; the Cu-T1 band at 580 nm ($\varepsilon \approx 5600$ M^{-1} cm^{-1}) was not detectable at 50 nM enzyme concentration). The spectra were also corrected for a small scattering background at longer wavelengths that developed as the reaction progressed.

We discovered that MnO_2 is sensitive to UV light (Figure S1 and discussion therein), especially in the presence of the HEPES buffer (whose side reactions are the subject of numerous warnings in the literature),[20,57−65] and that even the illumination from the spectrometer UV source had a small effect on the reaction time course. Consequently, for the final kinetic measurement, the UV lamp was turned off, and the spectral evolution was monitored in the 340−1000 nm region (Figure S2).

MCR-ALS analysis. After substrate addition, growth of the MnO_2 absorption band was accompanied by a red-shift. To separate growth and spectral shift, we applied multivariate analysis, using the MCR-ALS (Multivariate Curve Resolution−Alternating Least-Squares) algorithm developed and implemented as a graphical interface by Tauler et al.[66−68] and run in the MATLAB 8.3 environment (The MathWorks, Inc.). MCR-ALS is a well-established decomposition method to extract spectral and concentration profiles of absorbing species contributing to overlapping data without any assumptions about the composition of the system.[66] This algorithm, described previously,[68,69] has been successfully applied to a number of evolving multicomponent systems monitored by different techniques,[69−76] including analysis of time-dependent UV−vis spectra.[71,77,78]

Briefly, the time-resolved spectral data are arranged in a matrix $\mathbf{D}$ ($r \times c$), where rows r are the spectra collected at different times during the reaction and columns c are the kinetic traces collected at different wavelengths. The MCR decomposes the matrix $\mathbf{D}$ according to the equation

$$\mathbf{D} = \mathbf{C}\mathbf{S}^{\mathrm{T}} + \mathbf{E} \quad (1)$$

where the matrix $\mathbf{S}^{\mathrm{T}}$ ($n \times c$) contains the spectral profiles of n pure resolved components and the matrix $\mathbf{C}$ ($r \times n$) describes the concentration profiles of these n species. $\mathbf{E}$ ($r \times c$) is the residual matrix, which contains unexplained data variance. Initial guesses of the n spectral profiles are input to eq 1 in a constrained alternating least-squares (ALS) optimization procedure: initial $\mathbf{C}$ or $\mathbf{S}^{\mathrm{T}}$ guesses are refined to yield pure response profiles associated with the variation of each contribution in the row and the column directions. Optimization proceeds until the standard deviations of the residuals between experimental and calculated values falls below the specified value of 0.1% (Figure S3).

Singular value decomposition (SVD)[79] was initially used to find the number of significant components accounting for the variance in $\mathbf{D}$. Around 98% of the spectral changes resulted from just two components, whose spectral profiles resembled those of the earliest and latest experimental spectra, a conclusion supported by evolving factor analysis (EFA, as implemented in the updated MCR-ALS graphical user interface;[64,80,81] see captions to Figure S3B for description). Consequently, we used early and late experimental spectra as inputs to the MCR-ALS optimization, attributing the early spectrum to the initial enzyme product, and the late spectrum to the mature MnO_2 nanoparticles. Because the reaction ran to completion, the late spectral absorbance (such as the 350-s spectrum in Figure 3A, for example) provides the molar extinction coefficient. However, this coefficient is unknown for the early spectra; it was scaled to 80% of the final coefficient, based on our observations of the absorptivities of synthetic MnO_2 preparations of different particle sizes and absorption peak wavelengths (Figure S3C). The nanoparticle absorption spectrum, together with its extinction coefficient, is known to be a size-dependent quality,[82] as shown for different nanoparticles, for example, CdTe, CdSe, and CdS nanocrystals;[83] Au nanoparticles;[84,85] and PbSe nanocrystals.[86]

To obtain chemically meaningful results, two constraints were applied during the MCR-ALS procedure: one forcing the concentrations and the spectra to remain positive, and the other restricting both components to be less than or equal to the starting $MnSO_4$ concentration. The MCR-ALS analysis reproduced 99.9% of variances in the experimental data, resulting in a lack-of-fit (LOF) of less than 1% (Figure S3D; except for the 10 μM $MnSO_4$ data set, which had low signal-to-noise due to lower absorbance).

Type 1 Cu reduction potential measurements. Experiments to gauge the ability of Mn(II) to reduce the type 1 Cu (T1Cu) were carried out using a Cary 50 Bio UV−visible absorption spectrophotometer in a 1 cm path length anaerobic cuvette. First, 400 μL 25 μM as-isolated Mnx protein was deoxygenated by purging argon for 0.5 h and brought into a glovebox that had been purged with N_2. There, the Mnx protein was buffer exchanged with the O_2-free phosphate buffer (0.1 M sodium phosphate, pH 7.8) using Amicon Ultra centrifugal filter (30 kDa cutoff). The resulting 400 μL 25 μM Mnx protein was transferred into a 1 cm path length anaerobic cuvette to take an absorption spectrum. Then, to the cuvette, 7 equiv of Mn^{2+}(aq) (175 μL 400 μM degassed $MnSO_4$) was added using a gastight syringe (Hamilton). After anaerobic incubation for ∼1.5 h, an absorption spectrum was taken, followed by addition of 125 μL O_2-saturated phosphate buffer with the gastight syringe. After mixing for 15 min, an absorption spectrum was collected again.

The reduction potential of T1Cu in Mnx protein was measured by the poised potential titration method.[87] The Mn(II)-containing protein was titrated (at 25 °C) in the glovebox by adding ∼25 μL increments of deoxygenated 0.5 mM $K_3Fe(CN)_6$, with a gastight syringe. Absorption spectra were monitored after each increment until reaction was complete (∼15 min). A reductive titration was then carried out using 6 mM deoxygenated $K_4[Fe(CN)_6]$. The concentration of oxidized T1Cu was monitored via its absorbance, A, at 580 nm maximum, as $A/(A_0-A)$, where A_0 is the initial absorbance. The standard redox potential of the $K_4[Fe(CN)_6]/K_3[Fe(CN)_6]$ couple in

DOI: 10.1021/jacs.7b02771
J. Am. Chem. Soc. 2017, 139, 11369−11380

pH 7.8 phosphate buffer is ~430 mV. The standard potential reported in this paper is that determined at pH 7.8 and 25 °C.

RESULTS AND DISCUSSION

1. Mnx Is a Low-Potential MCO and Does Not Oxidize Mn(II) in the Absence of Oxygen. The reduction potential of the Mnx type 1 Cu center was measured by the poised potential titration method[88,89] with the $[Fe(CN)_6]^{3-}/[Fe(CN)_6]^{4-}$ redox couple.[87] The standard potential (at pH 7.8 and 25 °C) was determined via the Nernst equation (eq 2) for a one-electron process (n = 1).

$$E^0_{Fe^{2+/3+}} + \frac{2.3RT}{nF}\log\frac{[Fe^{3+}]}{[Fe^{2+}]} = E^0_{T1Cu^{+/2+}} + \frac{2.3RT}{nF}\log\frac{[T1Cu^{2+}]}{[T1Cu^{+}]} \quad (2)$$

The solution potential (left-hand side of eq 2) is set by the known $[Fe^{3+}]/[Fe^{2+}]$ ratio, and the standard potential of the $[Fe(CN)_6]^{3-}/[Fe(CN)_6]^{4-}$ redox couple, $E^0_{Fe^{2+/3+}}$ = 430 mV. A plot of the logarithm of the $[T1Cu^{2+}]/[T1Cu^{+}]$ ratio (see Methods section for details) resulted in a straight line with the expected slope, when plotted against the solution potential (Figure 2, inset). The intercept gave the value of $E^0_{T1Cu^{+/2+}}$ = 380 mV, at pH 7.8. Oxidative and reductive points fell on the same line, establishing reversibility.

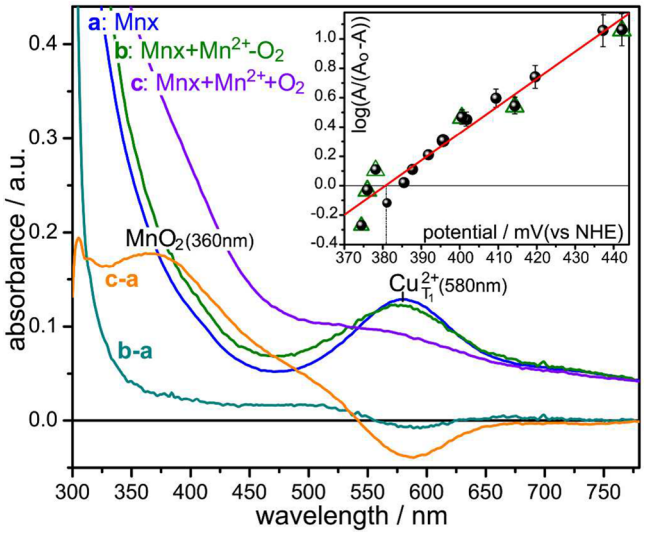

Figure 2. Absorption spectra of as-isolated Mnx protein (a, blue trace), and Mnx protein anaerobically incubated with 7 equiv of Mn^{2+}(aq) for ~1.5 h (b, green trace) and then mixed with O_2-saturated buffer solution for 15 min (c, purple trace). Subtracting trace a from trace b shows a small background and a negligible 580 nm absorption loss (dark cyan trace). A substantial 580 absorption loss is seen (orange trace) against the MnO_2 background absorption (maximum at ~360 nm) when trace a is subtracted from trace c. The spectrum b has been scaled by the dilution factor. The inset shows the plot of eq 2 for the poised potential titration of Mnx (black points and green triangles) and the linear correlation (red line, r = 0.978) with the x-intercept giving the reduction potential of T1Cu as 380 ± 5 mV (pH 7.8). The titration conditions were as follows: the black circles are starting with 0.5 mM $K_3[Fe(CN)_6]$ in pH 7.8 phosphate buffer and titrating with aliquots of 5 mM $K_4[Fe(CN)_6]$; the green triangles are starting with 0.5 mM $K_3[Fe(CN)_6]$ in pH 7.8 phosphate buffer and titrating with aliquots of 6 mM $K_4[Fe(CN)_6]$.

The type 1 Cu reduction potential ranges widely among MCOs (0.3–0.8 V[90–92]), and that of Mnx might have been expected to be quite high. Yet, our measured value, E^0 = 0.38 V (pH 7.8), is near the low end of the range. Indeed, the Mnx type 1 Cu is not reduced by Mn(II) in the absence of O_2. As shown in Figure 2, the 580 nm absorbance due to oxidized type 1 Cu was undiminished when Mnx was incubated anaerobically with Mn(II) (green trace b and b–a difference spectrum). When O_2 was admitted, producing the broad absorption due to MnO_2 (Figure 2, purple trace c), spectral subtraction of unreacted Mnx (Figure 2, orange c–a trace) gave a 580 nm dip in the MnO_2 background, revealing substantial reduction of the type 1 Cu during turnover. We infer that the enzyme requires activation, either to raise the type 1 Cu^{2+} reduction potential or to lower the Mn(III) reduction potential, in order to enable turnover. The type 1 Cu is in a rigid coordination environment (giving rise to the entatic/rack-induced state hypothesis[93–98]), and its E^0 is unlikely to be significantly affected by substrate binding. Below we present kinetic evidence that enzyme activation lowers the Mn(III) reduction potential via a novel binuclear mechanism.

2. Mnx Reaction Time Course: Separation of Enzymatic and Particle Aging Processes. To investigate the mechanism of Mn(II) oxidation, we employed UV–vis absorption spectroscopy to monitor Mnx-catalyzed product formation under varying conditions (Figure 1). The final product of Mn(II) oxidation by Mnx is MnO_2 mineral, resembling δ-MnO_2 hexagonal birnessite, as determined previously by X-ray absorption spectroscopy.[48] In UV–vis absorption spectra, the colloidal MnO_2 product is characterized by a broad ligand-to-metal charge transfer (LMCT) band centered at ~350 nm (Figure 3A), similar to the well-established spectrum of synthetic colloidal MnO_2.[99–103] (Scattering is minimal <600 nm, in the region of the monitored absorption band.[104,105]) The colloidal product was found not to precipitate, provided that salt is excluded from the buffer and that the starting Mn(II) concentration is kept below ~120 μM.[103,106] As the reaction progresses, the MnO_2 band grows, and also shifts to longer wavelengths (Figure 3A, inset), consistent with increasing particle size.[82,107,108] Thus, enzymatic oxidation and colloid aging occur on overlapping time scales. To disentangle these processes, we applied multivariate analysis to the time-dependent spectral profiles, as described in the Methods section. Two spectral components, S1 and S2, were found to account for 98% of the variance, and their profiles closely match the experimental spectra at early and late times (Figure 3A). Their progress curves (Figure 3B), computed after converting absorbances to concentrations (Methods), show the two components rising in sequence, S1 then falling while S2 rises to a final plateau. We attribute S1 to the enzyme product, likely a polynuclear Mn(IV) complex (see accompanying paper[54]), and S2 to MnO_2 nanoparticles formed by condensation of the enzyme product.

Following a lag phase (before any product appears), the initial portions of the two time courses each have a sigmoidal shape, rising to a linear region (Figure 3B).[109,110] For the enzymatic reaction, sigmoidal behavior is characteristic of enzyme activation,[111] while for the condensation process, it is characteristic of nucleation and particle growth.[112] The time courses were measured at a series of Mn(II) concentrations, pH values, and temperatures, in order to map out the kinetic parameters of the two processes and gain mechanistic insight. These parameters are gathered in Table 1.

DOI: 10.1021/jacs.7b02771
J. Am. Chem. Soc. 2017, 139, 11369–11380

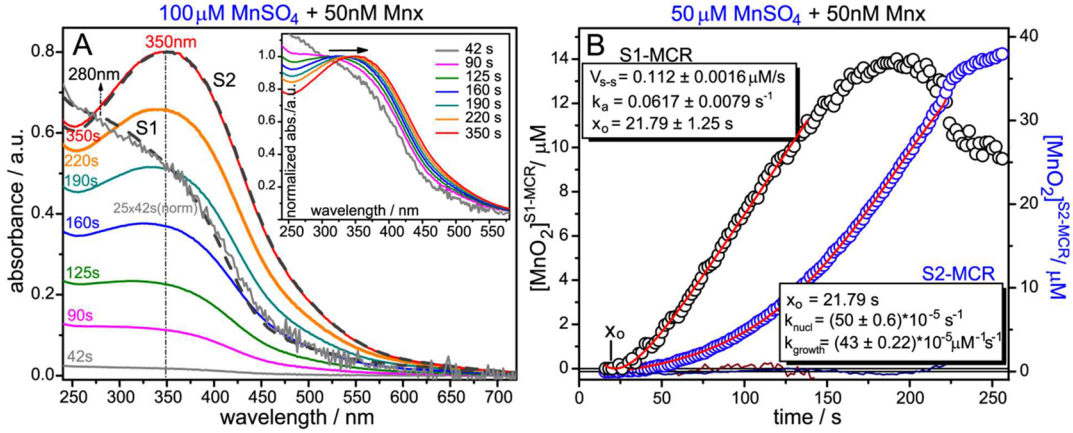

Figure 3. (A) UV−vis spectra taken at the indicated times during the Mnx-catalyzed oxidation of 100 μM $MnSO_4$ in 10 mM HEPES buffer, pH 7.8. The product of the reaction, nanoparticulate MnO_2, has a broad absorption band, which undergoes a red shift as it grows. The spectral profiles of the first (S1, black dashed line) and second (S2, black dashed line) components of the MCR-ALS multivariate analysis are superimposed on the normalized experimental spectra at 42 s (dark gray line) and 350 s (red line). *Inset*: The same UV−vis spectra on a normalized absorbance scale to show the red shift of the MnO_2 band more clearly. (B) Time profiles of the S1 (black points) and S2 (blue points) components obtained after the MCR-ALS procedure was applied to the data for 50 μM $MnSO_4$ and 50 nM Mnx in 10 mM HEPES, pH 7.8. (Only the visible light source was used, to avoid UV photoreaction of HEPES, see Figure S2 in SI.) The red line on top of the S1 component is the fit to the activation equation (eq 3), (r = 0.998), and the dark red line shows the residuals. The fitted time interval (up to 140 s) was selected before the slowing down of the steady-state rate due to substrate exhaustion. The red line on top of the S2 component is the fit to the agglomeration growth equation (eq 6) (r = 0.9994), and the dark blue line is the residual for the fit.

Table 1. Rate Parameters and Activation Energies Obtained for the Indicated Steps during 50 nM Mnx-Catalyzed Oxidation of $MnSO_4$ in 10 mM HEPES buffer[a]

Mn(II) binding					Mnx activation			Mnx turnover			MnO_2 nucl.		MnO_2 growth	
$k_{on}/\mu M^{-1}$ s^{-1}	k_{off}/s^{-1}	$K_d/\mu M$	E_a	$\Delta S^{\#}$	k_{act}/s^{-1}	E_a	$\Delta S^{\#}$	$V_{max}/\mu M$ s^{-1}	$\Delta G^{\#}_{cat}$	$\Delta S^{\#}$	E_a	$\Delta S^{\#}$	E_a	$\Delta S^{\#}$
0.00044	0.033	75	44	−128	0.059	106.4	87	0.2	66.2	34.6	70	−82	74.6	−64

[a] E_a is activation energy (in kJ/mol) estimated from Arrhenius plots, $\Delta S^{\#}$ is entropy from Eyring plots (in J/molK, see Figures S14A and S15 in SI), and $\Delta G^{\#}_{cat}$ (in kJ/mol) is activation energy of the catalyzed reaction during turnover.

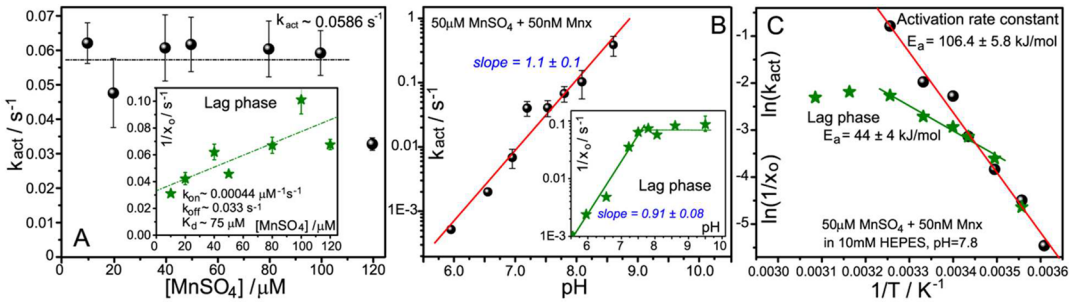

Figure 4. Dependence of the lag phase and activation rate constant parameters on (A) starting $MnSO_4$ concentration (in HEPES, pH 7.8), (B) pH (various buffers, 50 μM $MnSO_4$ starting concentration), and (C) temperature (50 μM $MnSO_4$ starting concentration, in HEPES, pH 7.8). (A) The activation rate constant is independent of $MnSO_4$ concentration, while the lag rate increases linearly, consistent with slow and weak (K_d = 75 μM) binding; the green line is the fit to eq 4, r = 0.793. (B) The log of the activation rate constant shows a unit-slope linear increase with pH (linear fit: r = 0.981), as does the lag rate, which, however levels off above pH 7.8 (linear fit: r = 0.988). (C) Arrhenius plots for the activation rate constant (black dots; linear fit: r = 0.993) and the lag rate (green stars; linear fit: r = 0.989).

3. The Enzyme Time Course. The induction and linear portions of the S1 time courses were fit to the equation for activated enzymes (eq 3),[111]

$$[MnO_2] = V_{s\text{-}s}(x - x_0) - \frac{V_{s\text{-}s}}{k_{act}}(1 - e^{-k_{act}(x-x_0)}) \quad (3)$$

where k_{act} is the rate constant for enzyme activation, and $V_{s\text{-}s}$ is the subsequent steady-state velocity. x_0 is the lag before reaction starts, and is optimized in the fitting procedure. The fits to eq 3 are collected in Figures 3B, S4, S10, and S13, and the dependencies of the extracted kinetic parameters on the starting Mn(II) concentrations, pH, and temperature are shown in Figures 4 and 5.

3.1. Lag Phase: Slow and Weak Mn(II) Binding. The lag phase before the start of the enzyme reaction was found to depend on Mn(II) concentration (Figure 4A, inset), reflecting Mn(II) substrate binding. A simple binding model predicts that the observed rate, $1/x_0$, is the sum of binding and dissociation rates (eq 4).

DOI: 10.1021/jacs.7b02771
J. Am. Chem. Soc. 2017, 139, 11369−11380

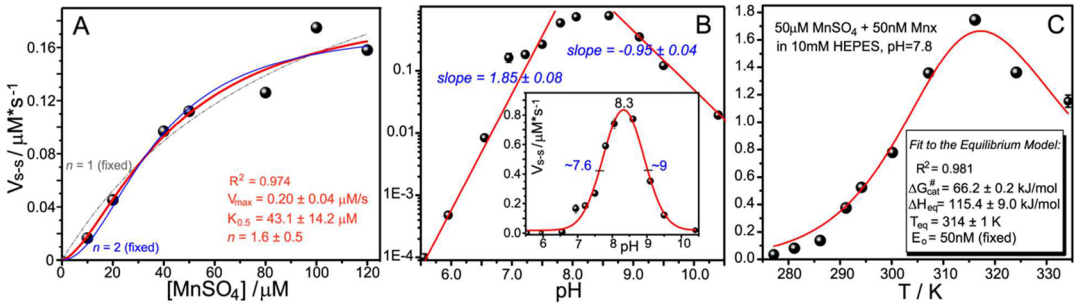

Figure 5. Dependence of the steady-state rate on (A) starting $MnSO_4$ concentration (in HEPES, pH 7.8), (B) pH (various buffers, 50 μM $MnSO_4$ starting concentration), and (C) temperature (50 μM $MnSO_4$ starting concentration, in HEPES, pH 7.8). (A) The steady-state rate shows Mn(II) cooperativity, following the Hill eq 5, with n = 1.6 (red line). Fixing n at 2 (blue line) gave a satisfactory fit, but fixing it at 1 (gray dotted line) did not. (B) The pH dependence is bell-shaped, with lower and upper pK_as of 7.6 and 9. The log plot shows a 2-proton transition at pK_a = 7.6 (linear fit: r = 0.996), and a 1-proton at pK_a = 9 (linear fit: r = 0.999). (C) The temperature dependence follows a model[113−115] (see equation (3) in SI) involving a reversible equilibrium between active and inactive forms, with equal concentrations at the temperature T_{eq}, and an equilibrium enthalpy ΔH_{eq}; $\Delta G^{\#}_{cat}$ is the activation free energy of the catalytic reaction.

$$\mathrm{Mnx} + \mathrm{Mn}^{2+} \underset{k_{-1}}{\overset{k_1}{\rightleftharpoons}} \mathrm{Mnx{-}Mn}^{2+}$$

$$1/x_0 = k_{obs} = k_1[\mathrm{Mn}^{2+}] + k_{-1} \quad (4)$$

A plot of the data is linear, giving binding and dissociation rate constants of ~0.00044 μM^{-1} s^{-1} and ~0.033 s^{-1}; their ratio is the dissociation equilibrium constant, a relatively high $K_d \approx 75$ μM. Measured as a function of pH, the lag rate is constant above pH 7.8, but decreases linearly below this value, with a slope of 1 (Figure 4B, inset). We infer that Mn(II) binding depends on deprotonation of a Mnx side chain with a pK of 7.8, likely a histidine. This side chain might bind directly to the Mn(II), or protonated histidine might block access to the binding site. The temperature dependence of the lag rate (Figure 4C, green stars) yields an activation energy of 44 kJ/mol, close to that reported for Fe^{2+} binding to apoferritin.[116]

Our earlier EPR study[117] provides insight into the Mnx-substrate binding event. Two distinct EPR signals for Mnx-bound Mn(II) were detected: one was a mononuclear signal, while the other arose from two weakly interacting Mn(II) ions. While the mononuclear and dinuclear sites might be separate, we suggest that there is a binuclear site which can be occupied by one or two Mn(II), depending on concentration. In the current study, only one Mn(II) binds to as-isolated Mnx, as demonstrated by the linear lag-rate dependence on [Mn(II)], and it binds weakly. The EPR spectra were obtained at a much higher concentrations of Mnx (25 μM vs 50 nM in the current study) and Mn(II), enabling a second Mn(II) to bind. The mixture of mono- and dinuclear signals suggests that K_d is even weaker for the second than the first Mn(II). However, the availability of two adjacent Mn(II) binding sites plays a key role in the mechanism we propose, based on the activation and turnover parameters, as presented below.

3.2. Activation Rate Constant: Mnx Activation through Mn(II)−OH⁻ Formation. The activation rate constant, k_{act}, is independent of Mn(II) concentration (Figure 4A), indicating that the substrate site is saturated in the activated enzyme, even at the lowest Mn(II) concentration employed, 10 μM. Thus, the as-isolated enzyme must undergo a conformation change upon activation to lower K_d from ~75 μM to ≪10 μM.[118] A key finding is that k_{act} increases logarithmically with pH, with a slope of 1 (Figure 4B), over the 6−8.6 pH range (above pH 8.6, the activation rate constant became too fast to resolve, Figure S10). This behavior implies that activation involves adding a hydroxide ion, or equivalently deprotonating a group with pK_a > 8.6. The likeliest candidate for this high pK_a is Mn(II)-bound water:

$$\mathrm{Mnx{-}Mn(II){-}OH_2} \rightarrow \mathrm{Mnx{-}Mn(II){-}OH^-} + \mathrm{H^+}$$

The pK_a of aquo-Mn(II) is 10.6,[119,120] and is unlikely to be greatly lowered by the coordinating groups at the MnxG active site. EPR and ESEEM spectroscopy of substrate-bound Mnx indicated two water molecules and one N per bound mononuclear Mn(II);[117] the remaining ligands are likely carboxylate, by analogy with multicopper ferroxidase substrate sites.[121−123] The pK_a of the water molecule bound to Mn(II) in MnSOD (superoxide dismutase; the remaining ligands being three His and one Asp in a trigonal bipyramidal environment),[124] has been calculated to be 9.0.[125]

The temperature dependence for k_{act} is steep (Figure 4C, black points), and yields a large activation enthalpy, 106 kJ/mol. This value is much higher than the 25−40 kJ/mol, typical for metal ion deprotonation in water, as estimated from the activation energies of water exchange processes for metal aqua complexes[126−129] or for enzyme-bound Mn(II),[130,131] and likely reflects a protein conformation change coupled to the Mn(II)−OH_2 deprotonation. An interesting precedent is offered by rhodopsin, which is activated by proton transfer from the retinal Schiff base to a protein acceptor, followed by conformation change of the protein. Activation energies of 160 and −60 kJ/mol have been determined for the two processes.[132,133] The net activation energy, 100 kJ/mol, is close to our value for k_{act}. The proposed Mnx conformation change is likely responsible for the increased Mn(II) affinity of the activated relative to the as-isolated enzyme, as noted above. We propose that affinity is also increased at an adjacent Mn(II) binding site, the one detected by EPR in as-isolated Mnx at high concentration.[117]

If the activation step operates through deprotonation of Mn(II)-bound water and enzyme conformation change, then the activation-linked hydroxide ion on the first Mn(II) would readily bridge to the second Mn(II). Hydroxide bridging of two manganese on the enzyme would provide a means of strongly diminishing the Mn(III)/Mn(II) reduction potential, as demonstrated by Dismukes et al. for a catalase model complex having two Mn(II) ions held in proximity by a binucleating polyamine ligand and a bridging carboxylate.[134] This complex underwent a two-electron oxidation at 790 mV vs SCE (in

DOI: 10.1021/jacs.7b02771
J. Am. Chem. Soc. 2017, 139, 11369−11380

acetone), but addition of one hydroxide equivalent lowered this high potential to ~350 and ~500 mV for two successive one-electron steps; the resulting complex showed anti-ferromagnetic coupling of the Mn(II) ions. Thus, hydroxide bridging produced a spin-coupled complex, in which the oxidation potential was lowered by 440 mV for the first Mn(II) and by 290 mV for the second, relative to the uncoupled complex without a hydroxide bridge. A nearly 0.5 V lowering could well bring the Mn(III)/Mn(II) reduction potential below the 0.38 V Cu(II)/Cu(I) potential of the Mnx type 1 Cu. We propose that hydroxide-bridging of two Mn(II) substrates, after the activation step, is the mechanism by which Mnx is enabled to oxidize Mn(II).

3.3. Mnx Turnover Involves Two Mn(II) and Two Deprotonations. The slow activation phase is followed by fast steady-state turnover of Mn(II). The steady-state rate, $V_{s\text{-}s}$, increases sigmoidally with starting Mn(II) concentration (Figure 5A), revealing Mn(II) cooperativity in turnover. The sigmoidal character agrees well with the curve obtained by Butterfield et al.[49,55] from oxidation measurements via a redox dye, although the rate constants differ because the activation step was not separated out in their analysis. Our data fit the Hill equation,[135]

$$V_{s\text{-}s} = \frac{V_{max}[MnSO_4]^n}{K_{0.5}^n + [MnSO_4]^n} \quad (5)$$

with $n = 1.6$. A satisfactory fit was also obtained with $n = 2$, but not with $n = 1$. Thus, enzyme turnover must involve two (or more) Mn(II) ions, the second reacting faster than the first. The maximum velocity, $V_{max} = 0.20$ μM/s, corresponds to a turnover number of 4 s^{-1} (dividing V_{max} by the Mnx concentration, 0.05 μM), which is in the 0.5−10 s^{-1} range observed for other MCO metalloxidases (ceruloplasmin, Fet3p, and CueO).[91,136−143]

The involvement of two Mn(II) ions in turnover dovetails with our proposal that Mnx is activated by Mn(II)−OH^- formation at the substrate site, inducing a conformation change that increases affinity for a second Mn(II). This second Mn(II) would be the initial Mn(II) taken up during turnover, since as argued above, a Mn(II)(μ-OH)Mn(II) complex lowers the Mn(III)/Mn(II) potential and induces electron transfer. The result would be formation of Mn(III), which would be expected to translocate to a distal site since the substrate site is tailored to a divalent ion. Notably, Lindley et al.[121] have shown via crystallographic soaking experiments that trivalent ions are excluded from the Fe(II) substrate site of the ferroxidase MCO ceruloplasmin, and instead bind at a more distant site, where the Fe(III) product is presumably held. Similarly, Mn(III) is excluded from the Mn(II) substrate site of Mnx, as demonstrated in our companion paper.[54]

The next electron transfer produces a second Mn(III), which could form another dinuclear complex Mn(III)(μ-$OH)_2$Mn(III), doubly bridged by OH^-. The enhanced stability of this complex would further reduce the Mn(III)/Mn(II) potential, and enhance the electron transfer rate, accounting for the faster reaction of the second turnover step. Support for this inference is provided by the pH dependence of $V_{s\text{-}s}$ (Figure 5B), which reveals an enabling deprotonation with $pK_a = 7.6$, as well as an inhibiting deprotonation with $pK_a = 9$. The log plot shows that the latter deprotonation involves a single proton, but the former involves two protons. While a $pK_a = 7.6$ deprotonation could arise from a protein side-chain, especially histidine, it is unlikely that two of them would be required to deprotonate simultaneously for catalysis. Instead we assign the $pK_a = 7.6$ deprotonation to Mn(III)-bound H_2O. While the pK_a of aquo-Mn(III), 0.08,[119,144] is much lower than this value, it is significantly modulated by coordinating ligands. For example, $pK_a = 9.2$ for deprotonation of water bound to Mn(III) phthalocyanine, while binding of pyridine as a *trans* ligand shifts it to $pK_a = 7.2$.[145] We note that in the tetranuclear Mn water oxidation complex of photosystem II, the pK_a for deprotonation to produce a hydroxy bridge between two Mn(III) has been estimated to be 7.1.[146] The formation of Mn(III)(μ-$OH)_2$Mn(III) during the second turnover would account for the observed double deprotonation at pH 7.6. In the accompanying paper[54] we present evidence that this species is the key intermediate in the ultimate formation of MnO_2. (The nature of the inhibiting $pK_a \approx 9$ deprotonation seen in the velocity/pH curve is uncertain, but presumably involves a side chain, likely a $LysH^+$ or TyrOH residue. Its deprotonation might inhibit subsequent steps in the reaction mechanism, or it might alter the active site structure, similarly to the inhibition of MnSOD activity upon deprotonation of a TyrOH residue near the active site.[147,148])

The temperature profile of the turnover rate (Figure 5C), with a temperature maximum, is characteristic of enzymes that have a reversible equilibrium between active and thermally inactivated forms.[113] A model has been developed[113−115] for this behavior (see equation (3) in SI) that permits estimation of the enthalpy change of the active/inactive equilibrium and the temperature, T_{eq}, at which the two forms are of equal concentration, as well as the activation energy for catalysis. The fitted parameters are indicated in Figure 5C. The Mnx turnover activation free energy, 66.2 kJ/mol, is in the middle of a range of values reported for a series of microbial enzymes (Table 1 in ref 115). The active/inactive enthalpy, 115 kJ/mol, is close to the activation energy of k_{act}, 106 kJ/mol, which, as discussed above, reflects the conformation change to the activated form of Mnx. It is possible that the active-inactive equilibrium reflects a high-temperature shift back toward the pre-activated conformation adopted by as-isolated Mnx.

4. Sigmoidal Time Course Is Not Due to Abiotic Autocatalysis. Since there are reports[4,149−152] of increased oxidation rates when Mn(II) adsorbs on MnO_2, we considered the possibility that the observed sigmoidal time course of MnO_2 formation might result from autocatalysis by abiotic oxidation of Mn(II) adsorbed on newly formed MnO_2 product. Direct measurement of the autocatalytic rate in the absence of enzyme are difficult; we found that synthetically prepared MnO_2 colloids precipitate when Mn(II) is added under the conditions of the enzymatic reaction (Figure S7), perhaps via comproportionation to a mixed-valence oxide,[4,64,151,153−155] or cation-induced coagulation (Figure S7B).[156,157]

However, a significant abiotic contribution to the enzymatic MnO_2 production was ruled out by successive additions of Mn(II) to the enzyme assay (Figure 6). Adding a second aliquot of Mn(II) after the initial MnO_2 signal has plateaued produces a fresh rise in the signal, which was resolved into S1 and S2 components (Figure S8) via the MCR-ALS method described above. The S1 (enzymatic) component rises hyperbolically, without lag or induction phases, indicating that the enzyme remains activated after the first round (Figures 6 and S8A). Fitting of the initial linear portion (Figure S8A) gives a turnover rate, $V_{s\text{-}s} = 0.043$ μM/s, in good agreement

DOI: 10.1021/jacs.7b02771
J. Am. Chem. Soc. 2017, 139, 11369−11380

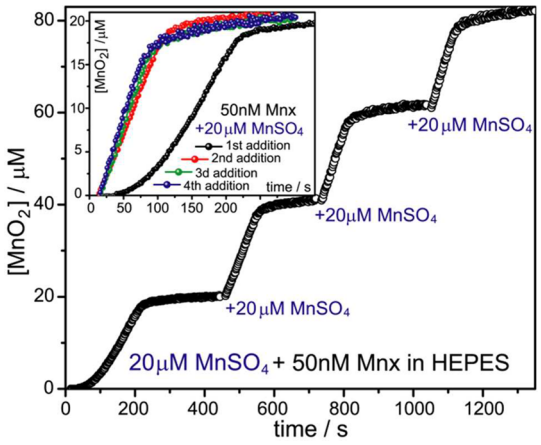

Figure 6. Time traces obtained during Mnx-catalyzed oxidation of four 20 μM $MnSO_4$ aliquots. Mn(II) substrate was added in four consecutive steps to the same cuvette (initially containing 50 nM Mnx in 10 mM HEPES buffer) without stopping data collection, with illumination from the vis lamp only. Each new plateau showed quantitative MnO_2 production, obtained using the extinction coefficient derived from the first plateau. *Inset*: The same time traces, shifted to time zero and brought down, to coincide with the start of the oxide formation from the first aliquot; otherwise no scaling or normalization was performed.

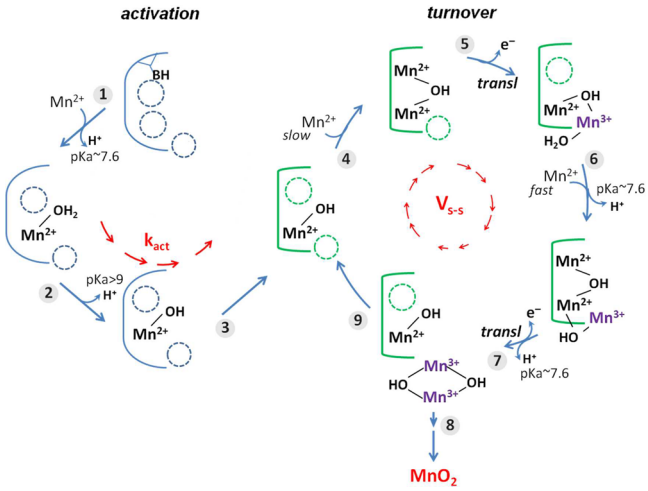

Figure 7. Proposed mechanism of Mnx activation and turnover. Deprotonation of a protein residue ($pK_a \approx 7.6$, likely $HisH^+$) allows Mn(II) binding at the substrate site, where a bound H_2O deprotonates ($pK_a > 9$), inducing enzyme conformation change and enzyme activation. Binding of a second Mn(II) is followed by OH^- bridging of the two Mn(II) ions, lowering the Mn(II) oxidation potential. Electron transfer to T1 Cu^{2+} generates Mn(III), which translocates to a distal site. Another Mn(II) binds to the vacated site, and deprotonation of the Mn(III) ($pK_a \approx 7.6$) allows formation of a new hydroxide bridge. Another sequence of electron transfer, Mn(III) translocation, and deprotonation produces a binuclear Mn(III) complex that proceeds to product, leaving activated enzyme to complete the cycle.

with the value obtained with as-isolated enzyme for 20 μM Mn(II) (Figure S4).

Importantly, further additions of a third and fourth aliquot reproduce the production time course of the second round (Figure 6, inset). Thus, the rate of reaction is independent of the amount of MnO_2 that has been produced. Had abiotic autocatalysis been significant, the rate of production would have increased with the concentration of preformed MnO_2. We conclude that under the assay conditions, MnO_2 production reflects oxidation by the enzyme alone.

The S2 component (nanoparticle formation and aging) of the second round (Figure S8B) showed much faster (5-fold) MnO_2 nucleation than the first round, since the precursor, the immediate enzyme product, is produced faster in the absence of an activation step. The nanoparticle growth rate of the second addition, however, was similar to that observed for as-isolated enzyme (see below).

5. Proposed Catalytic Mechanism. Putting together the results for Mnx substrate binding, activation, and turnover (sections 3.1−3.3 above), we propose the catalytic cycle diagrammed in Figure 7. The nine steps are as follows:

1. Mn(II) binds weakly to as-isolated Mnx; the binding is enabled by deprotonation of a $pK_a = 7.6$ side chain, likely histidine. A second site becomes available at high Mnx and Mn(II) concentration (EPR results[117]).
2. Activation involves deprotonation of the water bound to Mn(II) ($pK_a > 8.6$), and
3. an enzyme conformation change that increases Mn(II) affinity at both binding sites.
4. Mn(II) binding to the second site forms a hydroxide-bridged dinuclear complex, which lowers the Mn(III)/Mn(II) reduction potential sufficiently to permit
5. electron transfer to the type 1 Cu, producing Mn(III), which translocates to a distal site, where it deprotonates ($pK_a = 7.6$). This is the first turnover step.
6. Another Mn(II) binds at the vacated substrate site.
7. The subsequent electron transfer is accelerated by deprotonation of the second Mn(III), which condenses with the first Mn(III) to produce Mn(III)(μ-OH)$_2$Mn-(III).
8. In subsequent steps (elucidated in the accompanying paper[54]), this intermediate proceeds to MnO_2, while
9. The activated enzyme, retaining Mn(II)−OH^-, re-enters the catalytic cycle.

6. Nucleation and Growth of MnO_2 Nanoparticles. The sigmoidal time course of the second spectral component (Figure 3 and Figures S5, S11, and S16), attributed to condensation of the enzyme product into growing MnO_2 particles, can be fit to the equation for the Finke−Watzky two-step mechanism of nanoparticle nucleation followed by agglomerative growth,[112,158]

$$[P]_x = [A]_0 - \frac{(k_1 + k_2[A]_0)[A]_0}{k_2[A]_0 + k_1 e^{(k_1+k_2[A]_0)(x-x_0)}} \quad (6)$$

where k_1 (in s^{-1}) is the nucleation rate constant, k_2 (in μM^{-1} s^{-1}) is the agglomeration growth rate constant, and x_0 (in s) represents the start of the reaction. $[P]_x$ is the concentration of aged product at time x, and $[A]_0$ is the starting $MnSO_4$ concentration. The nuclei are formed from the enzyme product, and then grow by agglomeration (see Finney et al.[159] for descriptions of "agglomerative nucleation" and "agglomerative growth"). Several mechanisms of attachment are possible, and have been reviewed.[160−166] Our data provide no information on this issue. By "nucleation" we mean simply that primary particles (the enzyme product) aggregate and dissociate reversibly, producing a delay in the growth curve, until a critical size is reached, after which dissociation becomes unimportant, and growth proceeds linearly until the primary

DOI: 10.1021/jacs.7b02771
J. Am. Chem. Soc. 2017, 139, 11369−11380

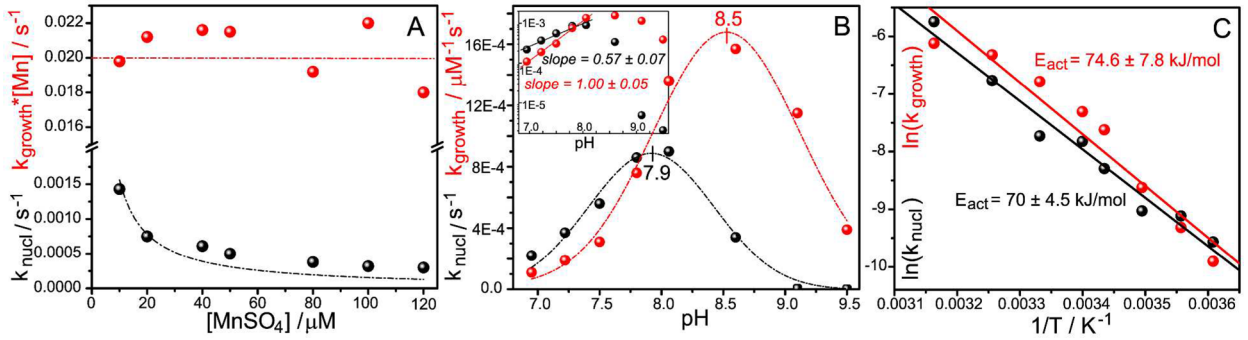

Figure 8. Dependence of the Mnx-produced nanoparticle nucleation (black points) and growth(agglomeration) (red points) rate constants on (A) starting $MnSO_4$ concentration (in HEPES, pH 7.8), (B) pH (various buffers, 50 μM $MnSO_4$ starting concentration), and (C) temperature (50 μM $MnSO_4$ starting concentration, in HEPES, pH 7.8). (A) The nucleation rate constant, k_{nucl}, is inversely dependent on the starting [Mn(II)], while the agglomeration growth rate, k_{growth}[Mn(II)], is independent of the starting [Mn(II)]. (B) The nucleation (black points) and growth (red points) rate constants [fits to the data shown in Figure S11] describe (see log(k) plots in the inset) bell curves with the indicated pH maxima. (C) Arrhenius plots for the nucleation (black points; fit: r = 0.987) and growth(agglomeration) (red points; fit: r = 0.968) rate constants [points obtained from the fits to the data shown in Figure S16].

particles are used up. This classical model is well documented in the nanoparticle literature.[162,167,168]

The rate parameters were determined at various starting Mn(II) concentrations (Figure S5), and the results (Figure 8A) show that the nucleation rate constant, k_1, is inversely dependent on [Mn(II)], as expected from the rate equation for the early stage of aggregation,[103,169−171]

$$k_1 \sim \frac{1}{N_o}\left(\frac{dD_h(t)}{dt}\right)_{t\to 0} \quad (7)$$

with k_1 proportional to the initial rate of increase in the hydrodynamic radius D_h and inversely proportional to the initial particle concentration N_0. In this case, the initial particles are the Mn(IV) complexes produced by the enzyme, whose concentration is proportional to the starting Mn(II) concentration. The ratio of growth and nucleation rate constants k_2[Mn(II)]/k_1, a predictor of nanoparticle size,[166] increases with starting Mn(II) concentration. The size of the final MnO_2 product is controlled by the nucleation stage: higher starting $MnSO_4$ concentrations lead to fewer nuclei and larger particles at the end of the reaction, consistent with the prediction of Finke et al.[160,172,173] Indeed, at higher starting $MnSO_4$ concentration, the final MnO_2 band shifts to longer wavelengths (Figure S6A), indicative of the formation of bigger particles.[82,107,108]

The pH dependence of the nucleation and growth rate constants is bell-shaped, with pH optima of 7.9 for nucleation and 8.5 for growth (Figure 8B).[174] As seen in a log plot (Figure 8B, inset), the pH dependence of the nucleation rate constant is much shallower than would be consistent with discrete protonation/deprotonation steps, and likely reflects processes dependent on the surface charge of the particles. Changes in buffer adsorption could provide a plausible mechanism. The HEPES buffer has a pK_a = 7.5, slightly below the pH optimum. Its conjugate acid is a protonated amine, whose pK_a would be raised by association with the negatively charged oxygen atoms on the MnO_2 particles. Adsorption might be stronger on the growing particles than on the polynuclear enzyme product that forms the nuclei, accounting for the shift in pH optima. The optima would reflect a balance between inhibition of aggregation due to increasing buffer cation adsorption on the low pH side, and increasing negative charge repulsion as the buffer cation concentration decreases on the high pH side. It is also possible that the lower pH optimum of the nucleation rate reflects ionic interactions at nucleation sites on the enzyme surface, where the polynuclear complex emerges.

When determined as a function of temperature, the rate constants for nucleation and growth gave linear Arrhenius (Figure 8C) and Eyring (Figure S15) plots, yielding activation energies and entropies that agree very well with reported parameters for other nanoparticles.[112,175,176] The activation enthalpies for nucleation (67 kJ/mol) and growth (72 kJ/mol) are similar, consistent with activation parameters found for other nanoparticles,[112,176] and the entropies are negative, −82 and −64 J/mol·K, respectively (Figure S15 and Table 1), as expected for associative processes.

We have no information on the role of the protein in controlling particle aggregation and growth. This intriguing issue is left for future studies.

■ CONCLUSIONS

MnxG is a novel MCO, having a low-potential type 1 Cu, despite being required to carry out an apparently high potential oxidation of Mn(II) to Mn(III). It circumvents this difficulty by exploiting the high sensitivity of the Mn(III)/Mn(II) reduction potential to the stabilizing effect of hydroxide formation and bridging. Uniquely among MCOs, MnxG has two Mn(II)-substrate binding sites. The kinetic analysis leads us to propose that the enzyme is activated by deprotonation of a Mn(II)-bound H_2O, coupled to a conformation change that induces hydroxide bridging to the second Mn(II), thereby dramatically lowering the Mn(III)/Mn(II) reduction potential so that electron transfer to the low-potential type 1 Cu is enabled.

Initial binding of Mn(II) is relatively slow and weak, but Mn(II) deprotonation in the activation step induces a shift to a high-affinity enzyme conformation. Binding and bridging of the second Mn(II) initiates turnover, and the resulting Mn(III) deprotonates. Turnover accelerates when still another Mn(II) binds, permitting formation of the binuclear intermediate Mn(III)(μ-OH)$_2$Mn(III). The nature of the second oxidation step, Mn(III) to Mn(IV), is analyzed in the accompanying paper,[54] where a full enzymatic mechanism is proposed.

The immediate enzyme product is likely Mn(IV)(μ-O)$_2$Mn-(IV), or an oligomer, from which MnO_2 nanoparticles nucleate

DOI: 10.1021/jacs.7b02771
J. Am. Chem. Soc. 2017, 139, 11369−11380

and grow in a classical manner. However, the role of the protein in guiding nanoparticle formation remains to be elucidated.

■ ASSOCIATED CONTENT

Supporting Information

The Supporting Information is available free of charge on the ACS Publications website at DOI: 10.1021/jacs.7b02771.

Stability tests of MnO_2 in HEPES buffer; description of the MCR-ALS fitting procedure applied to the time-resolved UV−vis spectroscopic data; dependencies of the final MnO_2 band and MnO_2 time courses on the assay conditions; collections of the fitted time courses of the MCR-ALS-resolved components, S1 and S2, to extract parameters used to plot $[MnSO_4]$-, pH-, and temperature dependencies in the main text; detailed description and results of the abiotic control and successive addition experiments; Equilibrium Model equation used to fit temperature dependence of the steady-state rate in Figure 5C; temperature dependencies of the fitted parameters in the Eyring form; and results of the CD experiment to probe enzyme conformation change (PDF)

■ AUTHOR INFORMATION

Corresponding Author

*spiro@chem.washington.edu

ORCID

Alexandra V. Soldatova: 0000-0003-2876-6262

William H. Casey: 0000-0002-3275-6465

R. David Britt: 0000-0003-0889-8436

Author Contributions

‡L.T. and C.A.R contributed equally to this work.

Notes

The authors declare no competing financial interest.

■ ACKNOWLEDGMENTS

This work was supported by the National Science Foundation: award numbers CHE-1410353 to T.G.S., CHE-1410688 to B.M.T., EAR-1231322 to W.H.C., and CHE-1213699 to R.D.B., and an NSF Postdoctoral Research Fellowship in Biology Award ID DBI-1202859 to C.A.R.

■ REFERENCES

(1) Tebo, B. M.; Johnson, H. A.; McCarthy, J. K.; Templeton, A. S. *Trends Microbiol.* **2005**, *13*, 421−428.

(2) Nealson, K. H.; Tebo, B. M.; Rosson, R. A. *Adv. Appl. Microbiol.* **1988**, *33*, 279−318.

(3) Tebo, B. M.; Bargar, J. R.; Clement, B.; Dick, G.; Murray, K. J.; Parker, D.; Verity, R.; Webb, S. M. *Annu. Rev. Earth Planet. Sci.* **2004**, *32*, 287−328.

(4) Learman, D. R.; Wankel, S. D.; Webb, S. M.; Martinez, N.; Madden, A. S.; Hansel, C. M. *Geochim. Cosmochim. Acta* **2011**, *75*, 6048−6063.

(5) Santelli, C. M.; Webb, S. M.; Dohnalkova, A. C.; Hansel, C. M. *Geochim. Cosmochim. Acta* **2011**, *75*, 2762−2776.

(6) Myers, C. R.; Nealson, K. H. *Science* **1988**, *240*, 1319−1321.

(7) Lovley, D. R. *Microbiol. Rev.* **1991**, *55*, 259−287.

(8) Lin, H.; Szeinbaum, N. H.; DiChristina, T. J.; Taillefert, M. *Geochim. Cosmochim. Acta* **2012**, *99*, 179−192.

(9) Morgan, J. J. *Geochim. Cosmochim. Acta* **2005**, *69*, 35−48.

(10) Tebo, B. M.; Ghiorse, W. C.; van Waasbergen, L. G.; Siering, P. L.; Caspi, R. In *Geomicrobiology: interactions between microbes and minerals*; Banfield, J. F., Nealson, K. H., Eds.; Mineralogical Society of America: Washington, DC, 1997; Vol. *35*, pp 225−266.

(11) Miyata, N.; Tani, Y.; Sakata, M.; Iwahori, K. *J. Biosci. Bioengin.* **2007**, *104*, 1−8.

(12) Emerson, D. In *Environmental Microbe-Metal Interactions*; Lovley, D. R., Ed.; American Society for Microbiology: Washington, DC, 2000.

(13) Brouwers, G.-J.; Vijgenboom, E.; Corstjens, P. L. A. M.; de Vrind, J. P. M.; de Vrind-de Jong, E. W. *Geomicrobiol. J.* **2000**, *17*, 1−24.

(14) Daly, M. J. *Nat. Rev. Microbiol.* **2009**, *7*, 237−245.

(15) Sunda, W. G.; Kieber, D. J. *Nature* **1994**, *367*, 62−64.

(16) Tebo, B. M.; Geszvain, K.; Lee, S. In *Geomicrobiology: Molecular and Environmental Perspective*; Barton, L. L., Mandl, M., Loy, A., Eds.; Springer: Berlin, 2010; pp 285−308.

(17) Geszvain, K.; Butterfield, C. N.; Davis, R. E.; Madison, A. S.; Lee, S.-W.; Parker, D. L.; Soldatova, A. V.; Spiro, T. G.; Luther, G. W., III; Tebo, B. M. *Biochem. Soc. Trans.* **2012**, *40*, 1244−1248.

(18) Davies, G. *Coord. Chem. Rev.* **1969**, *4*, 199−224.

(19) Klewicki, J. K.; Morgan, J. J. *Environ. Sci. Technol.* **1998**, *32*, 2916−2922.

(20) Kostka, J. E.; Luther, G. W.; Nealson, K. H. *Geochim. Cosmochim. Acta* **1995**, *59*, 885−894.

(21) Parker, D. L.; Sposito, G.; Tebo, B. M. *Geochim. Cosmochim. Acta* **2004**, *68*, 4809−4820.

(22) Trouwborst, R. E.; Clement, B. G.; Tebo, B. M.; Glazer, B. T.; Luther, G. W., III. *Science* **2006**, *313*, 1955−1957.

(23) Schnetger, B.; Dellwig, O. *J. Marine Syst.* **2012**, *90*, 23−30.

(24) Yakushev, E.; Pakhomova, S.; Sørenson, K.; Skei, J. *Mar. Chem.* **2009**, *117*, 59−70.

(25) Madison, A. S.; Tebo, B. M.; Mucci, A.; Sundby, B.; Luther, G. W., III *Science* **2013**, *341*, 875−878.

(26) Vance, C. K.; Miller, A.-F. *Biochemistry* **2001**, *40*, 13079−13087.

(27) Leveque, V. J.-P.; Vance, C. K.; Nick, H. S.; Silverman, D. N. *Biochemistry* **2001**, *40*, 10586−10591.

(28) Miller, A.-F. *Acc. Chem. Res.* **2008**, *41*, 501−510.

(29) Olson, T. L.; Williams, J. C.; Allen, J. P. *Biochim. Biophys. Acta, Bioenerg.* **2013**, *1827*, 914−922.

(30) Theil, E. C.; Tosha, T.; Behera, R. K. *Acc. Chem. Res.* **2016**, *49*, 784−791.

(31) Bradley, J. M.; Le Brun, N. E.; Moore, G. R. *J. Biol. Inorg. Chem.* **2016**, *21*, 13−28.

(32) Honarmand Ebrahimi, K.; Hagedoorn, P. L.; Hagen, W. R. *Chem. Rev.* **2015**, *115*, 295−326.

(33) Chasteen, N. D.; Harrison, P. M. *J. Struct. Biol.* **1999**, *126*, 182−194.

(34) Uebe, R.; Schüler, D. *Nat. Rev. Microbiol.* **2016**, *14*, 621−637.

(35) Barber-Zucker, S.; Zarivach, R. *ACS Chem. Biol.* **2017**, *12*, 13−22.

(36) Jones, S. R.; Wilson, T. D.; Brown, M. E.; Rahn-Lee, L.; Yu, Y.; Fredriksen, L. L.; Ozyamak, E.; Komeili, A.; Chang, M. C. Y. *Proc. Natl. Acad. Sci. U. S. A.* **2015**, *112*, 3904−3909.

(37) van Waasbergen, L. G.; Hildebrand, M.; Tebo, B. M. *J. Bacteriol.* **1996**, *178*, 3517−3530.

(38) Corstjens, P. L. A. M.; de Vrind, J. P. M.; Goosen, T.; de Vrind-de Jong, E. W. *Geomicrobiol. J.* **1997**, *14*, 91−108.

(39) Okazaki, M.; Sugita, T.; Shimizu, M.; Ohode, Y.; Iwamoto, K.; de Vrind-de Jong, E. W.; de Vrind, J. P. M.; Corstjens, P. L. A. M. *Appl. Environ. Microbiol.* **1997**, *63*, 4793−4799.

(40) Larsen, E. I.; Sly, L. I.; McEwan, A. G. *Arch. Microbiol.* **1999**, *171*, 257−264.

(41) Brouwers, G.-J.; de Vrind, J. P. M.; Corstjens, P. L. A. M.; Cornelis, P.; Baysse, C.; de Vrind-de Jong, E. W. *Appl. Environ. Microbiol.* **1999**, *65*, 1762−1768.

(42) Francis, C. A.; Tebo, B. M. *Appl. Environ. Microbiol.* **2002**, *68*, 874−880.

(43) Ridge, J. P.; Lin, M.; Larsen, E. I.; Fegan, M.; McEwan, A. G.; Sly, L. I. *Environ. Microbiol.* **2007**, *9*, 944−953.

DOI: 10.1021/jacs.7b02771
J. Am. Chem. Soc. 2017, 139, 11369−11380

(44) Dick, G. J.; Torpey, J. W.; Beveridge, T. J.; Tebo, B. M. *Appl. Environ. Microbiol.* **2008**, *74*, 1527−1534.
(45) Geszvain, K.; McCarthy, J. K.; Tebo, B. M. *Appl. Environ. Microbiol.* **2013**, *79*, 357−366.
(46) Solomon, E. I.; Sundaram, U. M.; Machonkin, T. E. *Chem. Rev.* **1996**, *96*, 2563−2605.
(47) Kosman, D. J. *J. Biol. Inorg. Chem.* **2010**, *15*, 15−28.
(48) Butterfield, C. N.; Soldatova, A. V.; Lee, S.-W.; Spiro, T. G.; Tebo, B. M. *Proc. Natl. Acad. Sci. U. S. A.* **2013**, *110*, 11731−11735.
(49) Butterfield, C. N. Characterizing the Mn(II) oxidizing enzyme from the marine Bacillus sp. PL-12 spore. Ph.D. Thesis, Oregon Health & Science University, Portland, OR, 2014.
(50) Romano, C. A.; Zhou, M.; Song, Y.; Wysocki, V.; Dohnalkova, A. C.; Kovarik, L.; Paša-Tolić, L.; Tebo, B. M. *Nat. Commun.* **2017**, submitted.
(51) The accessory proteins bind tightly, and attempts to separate them have not succeeded in producing functional MnxG.[52] However, small quantities of MnxG itself have recently been purified from an expression system containing only the *mnxG* gene.[53]
(52) Butterfield, C. N.; Tao, L.; Chacón, K. N.; Spiro, T. G.; Blackburn, N. J.; Casey, W. H.; Britt, R. D.; Tebo, B. M. *Biochim. Biophys. Acta, Proteins Proteomics* **2015**, *1854*, 1853−1859.
(53) Tao, L.; Stich, T. A.; Liou, S.-H.; Soldatova, A. V.; Delgadillo, D. A.; Romano, C. A.; Spiro, T. G.; Goodin, D. B.; Tebo, B. M.; Casey, W. H.; Britt, R. D. *J. Am. Chem. Soc.* **2017**, *139*, 8868−8877.
(54) Soldatova, A. V.; Romano, C.; Tao, L.; Stich, T. A.; Casey, W. H.; Britt, R. D.; Tebo, B. M.; Spiro, T. G. *J. Am. Chem. Soc.* **2017**, DOI: 10.1021/jacs.7b02772, (following paper in this issue).
(55) Butterfield, C. N.; Tebo, B. M. *Metallomics* **2017**, *9*, 183−191.
(56) Good, N. E.; Winget, G. D.; Winter, W.; Connolly, T. N.; Izawa, S.; Singh, R. M. M. *Biochemistry* **1966**, *5*, 467−477.
(57) Lepe-Zuniga, J. L.; Zigler, J. S., Jr.; Gery, I. *J. Immunol. Methods* **1987**, *103*, 145.
(58) Zigler, J. S.; Lepe-Zuniga, J. L.; Vistica, B.; Gery, I. *In Vitro* **1985**, *21*, 282−287.
(59) Grady, J. K.; Chasteen, N. D.; Harris, D. C. *Anal. Biochem.* **1988**, *173*, 111−115.
(60) Morris, J. J.; Zinser, E. R. *J. Phycol.* **2013**, *49*, 1223−1228.
(61) Zhao, G.; Chasteen, N. D. *Anal. Biochem.* **2006**, *349*, 262−267.
(62) Hegetschweiler, K.; Saltman, P. *Inorg. Chem.* **1986**, *25*, 107−109.
(63) Kirsch, M.; Lomonosova, E. E.; Korth, H.-G.; Sustmann, R.; de Groot, H. *J. Biol. Chem.* **1998**, *273*, 12716−12724.
(64) Elzinga, E. J.; Kustka, A. B. *Environ. Sci. Technol.* **2015**, *49*, 4310−4316.
(65) Ferreira, C. M. H.; Pinto, I. S. S.; Soares, E. V.; Soares, H. V. M *RSC Adv.* **2015**, *5*, 30989−31003.
(66) Tauler, R.; Smilde, A.; Kowalski, B. *J. Chemom.* **1995**, *9*, 31−58.
(67) Jaumot, J.; Gargallo, R.; de Juan, A.; Tauler, R. *Chemom. Intell. Lab. Syst.* **2005**, *76*, 101−110.
(68) Jaumot, J.; de Juan, A.; Tauler, R. *Chemom. Intell. Lab. Syst.* **2015**, *140*, 1−12.
(69) de Juan, A.; Tauler, R. *Crit. Rev. Anal. Chem.* **2006**, *36*, 163−176.
(70) Ruckebusch, C.; Blanchet, L. *Anal. Chim. Acta* **2013**, *765*, 28−36.
(71) Wang, Y.; Ni, Y. *Talanta* **2014**, *119*, 320−330.
(72) Felten, J.; Hall, H.; Jaumot, J.; Tauler, R.; de Juan, A.; Gorzsás, A. *Nat. Protoc.* **2015**, *10*, 217−240.
(73) Blobel, J.; Bernadó, P.; Svergun, D. I.; Tauler, R.; Pons, M. *J. Am. Chem. Soc.* **2009**, *131*, 4378−4386.
(74) Wehrens, R.; Carvalho, E.; Masuero, D.; de Juan, A.; Martens, S. *Anal. Bioanal. Chem.* **2013**, *405*, 5075−5086.
(75) Kandelbauer, A.; Kessler, W.; Kessler, R. W. *Anal. Bioanal. Chem.* **2008**, *390*, 1303−1315.
(76) Sandroni, M.; Maufroy, A.; Rebarz, M.; Pellegrin, Y.; Blart, E.; Ruckebusch, C.; Poizat, O.; Sliwa, M.; Odobel, F. *J. Phys. Chem. C* **2014**, *118*, 28388−28400.
(77) Garrido, M.; Rius, F. X.; Larrechi, M. S. *Anal. Bioanal. Chem.* **2008**, *390*, 2059−2066.
(78) Hormozi-Nezhad, M. R.; Jalali-Heravi, M.; Kafrashi, F. *J. Chemom.* **2013**, *27*, 353−358.
(79) Golub, G. H.; Reinsch, C. *Numer. Math.* **1970**, *14*, 403−420.
(80) Gampp, H.; Maeder, M.; Meyer, C. J.; Zuberbühler, A. D. *Talanta* **1985**, *32*, 1133−1139.
(81) Maeder, M. *Anal. Chem.* **1987**, *59*, 527−530.
(82) Burda, C.; Chen, X.; Narayanan, R.; El-Sayed, M. A. *Chem. Rev.* **2005**, *105*, 1025−1102.
(83) Yu, W. W.; Qu, L.; Guo, W.; Peng, X. *Chem. Mater.* **2003**, *15*, 2854−2860.
(84) Jain, P. K.; Lee, K. S.; El-Sayed, I. H.; El-Sayed, M. A. *J. Phys. Chem. B* **2006**, *110*, 7238−7248.
(85) Liu, X.; Atwater, M.; Wang, J.; Huo, Q. *Colloids Surf., B* **2007**, *58*, 3−7.
(86) Dai, Q.; Wang, Y.; Li, X.; Zhang, Y.; Pellegrino, D. J.; Zhao, M.; Zou, B.; Seo, J.-T.; Wang, Y.; Yu, W. W. *ACS Nano* **2009**, *3*, 1518−1524.
(87) Nakamura, T. *Biochim. Biophys. Acta* **1958**, *30*, 44−52.
(88) Protein film electrochemistry was employed previously to measure Mnx redox properties,[89] but only the type 2 Cu reduction was observed; the type 1 Cu was apparently not accessible to the electrode.
(89) Tao, L.; Simonov, A. N.; Romano, C. A.; Butterfield, C. N.; Fekete, M.; Tebo, B. M.; Bond, A. M.; Spiccia, L.; Martin, L. L.; Casey, W. H. *Chem. - Eur. J.* **2017**, *23*, 1346−1352.
(90) Jones, S. M.; Solomon, E. I. *Cell. Mol. Life Sci.* **2015**, *72*, 869−883.
(91) Machonkin, T. E.; Quintanar, L.; Palmer, A. E.; Hassett, R.; Severance, S.; Kosman, D. J.; Solomon, E. I. *J. Am. Chem. Soc.* **2001**, *123*, 5507−5517.
(92) Solomon, E. I.; Kjaergaard, C. H.; Heppner, D. E. In *Electrochemical Processes in Biological Systems*; Lewenstam, A., Gorton, L., Eds.; Wiley: Hoboken, NJ, 2015.
(93) Vallee, B. L.; Williams, R. J. P. *Proc. Natl. Acad. Sci. U. S. A.* **1968**, *59*, 498−505.
(94) Solomon, E. I.; Hare, J. W.; Gray, H. B. *Proc. Natl. Acad. Sci. U. S. A.* **1976**, *73*, 1389−1393.
(95) Gray, H. B.; Malmström, B. G.; Williams, R. J. *J. Biol. Inorg. Chem.* **2000**, *5*, 551−559.
(96) Solomon, E. I.; Hadt, R. G. *Coord. Chem. Rev.* **2011**, *255*, 774−789.
(97) Zaballa, M.-E.; Abriata, L. A.; Donaire, A.; Vila, A. J. *Proc. Natl. Acad. Sci. U. S. A.* **2012**, *109*, 9254−9259.
(98) Perez-Henarejos, S. A.; Alcaraz, L. A.; Donaire, A. *Arch. Biochem. Biophys.* **2015**, *584*, 134−148.
(99) Lume-Pereira, C.; Baral, S.; Henglein, A.; Janata, E. *J. Phys. Chem.* **1985**, *89*, 5772−5718.
(100) Baral, S.; Lume-Pereira, C.; Janata, E.; Henglein, A. *J. Phys. Chem.* **1985**, *89*, 5779−5783.
(101) Sakai, N.; Ebina, Y.; Takada, K.; Sasaki, T. *J. Phys. Chem. B* **2005**, *109*, 9651−9655.
(102) Jaganyi, D.; Altaf, M.; Wekesa, I. *Appl. Nanosci.* **2013**, *3*, 329−333.
(103) Huangfu, X.; Jiang, J.; Ma, J.; Liu, Y.; Yang, J. *Environ. Sci. Technol.* **2013**, *47*, 10285−10292.
(104) Perez-Benito, J. F.; Arias, C. *J. Colloid Interface Sci.* **1992**, *152*, 70−84.
(105) Siebecker, M.; Madison, A. S.; Luther, G. W., III *Aquat. Geochem.* **2015**, *21*, 143−158.
(106) Higher concentrations of the enzyme were found to produce more stable colloids at higher starting $MnSO_4$ concentrations, perhaps due to stabilizing protein−mineral interactions.[103]
(107) Mullaugh, K. M.; Luther, G. W., III. *J. Environ. Monit.* **2010**, *12*, 890−897.
(108) Brus, L. E. *J. Chem. Phys.* **1984**, *80*, 4403−4409.
(109) We considered the possibility that the lag phase could be due to slow conversion of the as-isolated enzyme to the "native intermediate" known to be the oxidized form of MCOs during turnover.[110] However, the rate of this conversion[110] is much faster

DOI: 10.1021/jacs.7b02771
J. Am. Chem. Soc. 2017, 139, 11369−11380

than the Mnx lag time, and would not depend on the Mn(II) concentration, as is observed.
(110) Heppner, D. E.; Kjaergaard, C. H.; Solomon, E. I. *J. Am. Chem. Soc.* **2013**, *135*, 12212−12215.
(111) Frieden, C. *J. Biol. Chem.* **1970**, *245*, 5788−5799.
(112) Watzky, M. A.; Finke, R. G. *J. Am. Chem. Soc.* **1997**, *119*, 10382−10400.
(113) Peterson, M. E.; Eisenthal, R.; Danson, M. J.; Spence, A.; Daniel, R. M. *J. Biol. Chem.* **2004**, *279*, 20717−20722.
(114) Peterson, M. E.; Daniel, R. M.; Danson, M. J.; Eisenthal, R. *Biochem. J.* **2007**, *402*, 331−337.
(115) Daniel, R. M.; Danson, M. J.; Eisenthal, R.; Lee, C. K.; Peterson, M. E. *Extremophiles* **2008**, *12*, 51−59.
(116) Sun, S.; Chasteen, N. D. *J. Biol. Chem.* **1992**, *267*, 25160−25166.
(117) Tao, L.; Stich, T. A.; Butterfield, C. N.; Romano, C.; Spiro, T. G.; Tebo, B. M.; Casey, W. H.; Britt, R. D. *J. Am. Chem. Soc.* **2015**, *137*, 10563−10575.
(118) To probe for a conformation change, we recorded the Mnx CD spectrum, before and after MnO_2 production from Mn(II) (Figure S17). The negative 222 nm signal, which is characteristic of an α-helix, showed a ∼5% decrease. Since Mnx is a large multiprotein complex, this represents a significant structural change. However, further work is needed to confirm and extend this preliminary result.
(119) Li, J.; Fisher, C. L.; Chen, J. L.; Bashford, D.; Noodleman, L. *Inorg. Chem.* **1996**, *35*, 4694−4702.
(120) Jerome, S. V.; Hughes, T. F.; Friesner, R. A. *J. Phys. Chem. B* **2014**, *118*, 8008−8016.
(121) Lindley, P. F.; Card, G.; Zaitseva, I.; Zaitsev, V.; Reinhammar, B.; Selin-Lindgren, E.; Yoshida, K. *J. Biol. Inorg. Chem.* **1997**, *2*, 454−463.
(122) Taylor, A. B.; Stoj, C. S.; Ziegler, L.; Kosman, D. J.; Hart, P. J. *Proc. Natl. Acad. Sci. U. S. A.* **2005**, *102*, 15459−15464.
(123) Quintanar, L.; Gebhard, M.; Wang, T. P.; Kosman, D. J.; Solomon, E. I. *J. Am. Chem. Soc.* **2004**, *126*, 6579−6589.
(124) Edwards, R. A.; Baker, H. M.; Whittaker, M. M.; Whittaker, J. W.; Jameson, G. B.; Baker, E. N. *J. Biol. Inorg. Chem.* **1998**, *3*, 161−171.
(125) Fisher, C. L.; Chen, J.-L.; Li, J.; Bashford, D.; Noodleman, L. *J. Phys. Chem.* **1996**, *100*, 13498−13505.
(126) Swaddle, T. W.; Merbach, A. E. *Inorg. Chem.* **1981**, *20*, 4212−4216.
(127) Helm, L.; Nicolle, G. M.; Merbach, A. E. *Adv. Inorg. Chem.* **2005**, *57*, 327−379.
(128) Nordin, J. P.; Sullivan, D. J.; Phillips, B. L.; Casey, W. H. *Inorg. Chem.* **1998**, *37*, 4760−4763.
(129) Dees, A.; Zahl, A.; Puchta, R.; van Eikema Hommes, N. J. R.; Heinemann, F. W.; Ivanovic-Burmazovic, I. *Inorg. Chem.* **2007**, *46*, 2459−2470.
(130) Reuben, J.; Cohn, M. *J. Biol. Chem.* **1970**, *245*, 6539−6546.
(131) Gale, E. M.; Zhu, J.; Caravan, P. *J. Am. Chem. Soc.* **2013**, *135*, 18600−18608.
(132) Arnis, S.; Hofmann, K. P. *Proc. Natl. Acad. Sci. U. S. A.* **1993**, *90*, 7849−7853.
(133) Knierim, B.; Hofmann, K. P.; Ernst, O. P.; Hubbell, W. L. *Proc. Natl. Acad. Sci. U. S. A.* **2007**, *104*, 20290−20295.
(134) Boelrijk, A. E. M.; Khangulov, S. V.; Dismukes, G. C. *Inorg. Chem.* **2000**, *39*, 3009−3019.
(135) Segel, I. H. *Enzyme kinetics: Behavior and Analysis of Rapid Equilibrium and Steady-State Enzyme Systems*; Wiley-Interscience: New York, 1993.
(136) Osaki, S. *J. Biol. Chem.* **1966**, *241*, 5053−5059.
(137) Farver, O.; Bendahl, L.; Skov, L. K.; Pecht, I. *J. Biol. Chem.* **1999**, *274*, 26135−26140.
(138) Hassett, R. F.; Yuan, D. S.; Kosman, D. J. *J. Biol. Chem.* **1998**, *273*, 23274−23282.
(139) Stoj, C.; Kosman, D. J. *FEBS Lett.* **2003**, *554*, 422−426.
(140) Stoj, C. S.; Augustine, A. J.; Zeigler, L.; Solomon, E. I.; Kosman, D. J. *Biochemistry* **2006**, *45*, 12741−12749.
(141) Singh, S. K.; Grass, G.; Rensing, C.; Montfort, W. R. *J. Bacteriol.* **2004**, *186*, 7815−7817.
(142) Ziegler, L.; Terzulli, A.; Gaur, R.; McCarthy, R.; Kosman, D. J. *Mol. Microbiol.* **2011**, *81*, 473−485.
(143) Djoko, K. Y.; Chong, L. X.; Wedd, A. G.; Xiao, Z. *J. Am. Chem. Soc.* **2010**, *132*, 2005−2015.
(144) Sisley, M. J.; Jordan, R. B. *Inorg. Chem.* **2006**, *45*, 10758−10763.
(145) Blakemore, J. D.; Hull, J. F.; Crabtree, R. H.; Brudvig, G. W. *Dalton Trans.* **2012**, *41*, 7681−7688.
(146) Takaoka, T.; Sakashita, N.; Saito, K.; Ishikita, H. *J. Phys. Chem. Lett.* **2016**, *7*, 1925−1932.
(147) Jackson, T. A.; Xie, J.; Yikilmaz, E.; Miller, A.-F.; Brunold, T. C. *J. Am. Chem. Soc.* **2002**, *124*, 10833−10845.
(148) Maliekal, J.; Karapetian, A.; Vance, C.; Yikilmaz, E.; Wu, Q.; Jackson, T.; Brunold, T. C.; Spiro, T. G.; Miller, A.-F. *J. Am. Chem. Soc.* **2002**, *124*, 15064−15075.
(149) Kessick, M. A.; Morgan, J. J. *Environ. Sci. Technol.* **1975**, *9*, 157−159.
(150) Hem, J. D. *Geochim. Cosmochim. Acta* **1981**, *45*, 1369−1374.
(151) Perez-Benito, J. F. *J. Colloid Interface Sci.* **2002**, *248*, 130−135.
(152) Bargar, J. R.; Tebo, B. M.; Bergmann, U.; Webb, S. M.; Glatzel, P.; Chiu, V. Q.; Villalobos, M. *Am. Mineral.* **2005**, *90*, 143−154.
(153) Elzinga, E. J. *Environ. Sci. Technol.* **2011**, *45*, 6366−6372.
(154) Junta, J. L.; Hochella, M. F. *Geochim. Cosmochim. Acta* **1994**, *58*, 4985−4999.
(155) Zhao, H.; Zhu, M.; Li, W.; Elzinga, E. J.; Villalobos, M.; Liu, F.; Zhang, J.; Feng, X.; Sparks, D. L. *Environ. Sci. Technol.* **2016**, *50*, 1750−1758.
(156) Morgan, J. J.; Stumm, W. *J. Colloid Sci.* **1964**, *19*, 347−359.
(157) Perez-Benito, J. F. *Colloids Surf., A* **2003**, *225*, 145−152.
(158) Watzky, M. A.; Finke, R. G. *Chem. Mater.* **1997**, *9*, 3083−3095.
(159) Finney, E. E.; Shields, S. P.; Buhro, W. E.; Finke, R. G. *Chem. Mater.* **2012**, *24*, 1718−1725.
(160) Thanh, N. T. K.; Maclean, N.; Mahiddine, S. *Chem. Rev.* **2014**, *114*, 7610−7630.
(161) Li, D.; Nielsen, M. H.; Lee, J. R. I.; Frandsen, C.; Banfield, J. F.; De Yoreo, J. J. *Science* **2012**, *336*, 1014.
(162) Nielsen, M. H.; Li, D.; Zhang, H.; Aloni, S.; Han, T. Y.-J.; Frandsen, C.; Seto, J.; Banfield, J. F.; Cölfen, H.; De Yoreo, J. J. *Microsc. Microanal.* **2014**, *20*, 425−436.
(163) Banfield, J. F.; Welch, S. A.; Zhang, H.; Thomsen Ebert, T.; Penn, R. L. *Science* **2000**, *289*, 751−754.
(164) Polte, J. *CrystEngComm* **2015**, *17*, 6809−6830.
(165) Lee, J.; Yang, J.; Kwon, S. G.; Hyeon, T. *Nat. Rev. Mater.* **2016**, *1*, 16034.
(166) Finney, E. E.; Finke, R. G. *J. Colloid Interface Sci.* **2008**, *317*, 351−374.
(167) Chen, X.; Schröder, J.; Hauschild, S.; Rosenfeldt, S.; Dulle, M.; Förster, S. *Langmuir* **2015**, *31*, 11678−11691.
(168) Kashchiev, D. *Nucleation: Basic Theory with Applications*; Butterworths-Heinemann: Oxford, UK, 1999.
(169) Holthoff, H.; Egelhaaf, S. U.; Borkovec, M.; Schurtenberger, P.; Sticher, H. *Langmuir* **1996**, *12*, 5541−5549.
(170) Huynh, K. A.; Chen, K. L. *Environ. Sci. Technol.* **2011**, *45*, 5564−5571.
(171) Chen, K. L.; Elimelech, M. *Langmuir* **2006**, *22*, 10994−11001.
(172) Besson, C.; Finney, E. E.; Finke, R. G. *J. Am. Chem. Soc.* **2005**, *127*, 8179−8184.
(173) Watzky, M. A.; Finney, E. E.; Finke, R. G. *J. Am. Chem. Soc.* **2008**, *130*, 11959−11969.
(174) The parameters are unavailable for pH values below 7, because the enzyme reaction becomes slower than particle growth, thus determining the overall time course, which no longer shows a red-shift.
(175) Ott, L. S.; Finke, R. G. *Chem. Mater.* **2008**, *20*, 2592−2601.
(176) Finney, E. E.; Finke, R. G. *Chem. Mater.* **2008**, *20*, 1956−1970.

DOI: 10.1021/jacs.7b02771
J. Am. Chem. Soc. 2017, 139, 11369−11380